

# Chimera states in mechanical oscillator networks

Erik Andreas Martens<sup>a,b,1,2</sup>, Shashi Thutupalli<sup>c,d,1,2</sup>, Antoine Fourrière<sup>c</sup>, and Oskar Hallatschek<sup>a,e</sup>

<sup>a</sup>Group of Biophysics and Evolutionary Dynamics and <sup>c</sup>Department of Dynamics of Complex Fluids, Max Planck Institute for Dynamics and Self-Organization, 37077 Göttingen, Germany; <sup>b</sup>Centre for Ocean Life, National Institute for Aquatic Resources, Technical University of Denmark, 2800 Kongens Lyngby, Denmark; <sup>d</sup>Departments of Physics and Mechanical and Aerospace Engineering, Princeton University, Princeton, NJ 08544; and <sup>e</sup>Department of Physics, University of California, Berkeley, CA 94720

Edited\* by Boris I. Shraiman, University of California, Santa Barbara, CA, and approved May 10, 2013 (received for review February 14, 2013)

The synchronization of coupled oscillators is a fascinating manifestation of self-organization that nature uses to orchestrate essential processes of life, such as the beating of the heart. Although it was long thought that synchrony and disorder were mutually exclusive steady states for a network of identical oscillators, numerous theoretical studies in recent years have revealed the intriguing possibility of “chimera states,” in which the symmetry of the oscillator population is broken into a synchronous part and an asynchronous part. However, a striking lack of empirical evidence raises the question of whether chimeras are indeed characteristic of natural systems. This calls for a palpable realization of chimera states without any fine-tuning, from which physical mechanisms underlying their emergence can be uncovered. Here, we devise a simple experiment with mechanical oscillators coupled in a hierarchical network to show that chimeras emerge naturally from a competition between two antagonistic synchronization patterns. We identify a wide spectrum of complex states, encompassing and extending the set of previously described chimeras. Our mathematical model shows that the self-organization observed in our experiments is controlled by elementary dynamical equations from mechanics that are ubiquitous in many natural and technological systems. The symmetry-breaking mechanism revealed by our experiments may thus be prevalent in systems exhibiting collective behavior, such as power grids, optomechanical crystals, or cells communicating via quorum sensing in microbial populations.

ensemble dynamics | statistical physics | nonlinear dynamics

In 1665, Christiaan Huygens observed that two pendulum clocks suspended on a beam always ended up swinging in exact anti-phase motion (1) regardless of each pendulum’s initial displacement. He explained this self-emergent synchronization as resulting from the coupling between the clocks, which was mediated by vibrations traveling across the beam. Huygens’ serendipitous discovery has inspired many studies to establish that self-emergent synchronization is a central process to a spectacular variety of natural systems, including the beating of the heart (2), flashing fireflies (3), pedestrians on a bridge locking their gait (4), circadian clocks in the brain (5), superconducting Josephson junctions (6), chemical oscillations (7, 8), metabolic oscillations in yeast cells (9), and life cycles of phytoplankton (10).

Ten years ago, the dichotomy between synchrony and disorder was challenged by a theoretical study revealing that a population of identical coupled oscillators can attain a state where one part synchronizes and the other oscillates incoherently (11–23). These “chimera states” (13) emerge when the oscillators are coupled nonlocally (i.e., the coupling strength decays with distance between oscillators), which is a realistic scenario in many situations, including Josephson junction arrays (24) or ocular dominance stripes (25). Chimera states are counterintuitive because they occur even when units are identical and coupled symmetrically; however, with local or global coupling, identical oscillators either synchronize or oscillate incoherently but never do both simultaneously.

Since their discovery, numerous analytical studies (13, 14, 16–18) involving different network topologies (14, 19, 20) and various sources of random perturbations (21, 22) have established

chimeras as a robust theoretical concept and suggest that they exist in complex systems in nature with nonlocal interactions. However, experimental evidence for chimeras has been particularly sparse so far, and it has only been achieved recently via computer-controlled feedback (26, 27). This raises the question of whether chimeras can only be produced under very special conditions or whether they arise via generic physical mechanisms. Uncovering such physical mechanisms requires analytically tractable experiments with direct analogs to natural systems.

Our mechanical experiment shows that chimera states emerge naturally without the need to fine-tune interactions. We implement the simplest form of nonlocal coupling that can be achieved using a hierarchical network with two subpopulations (14, 15): Within each subpopulation, oscillators are coupled strongly, whereas the coupling strength between the two subpopulations is weaker. We place  $N$  identical metronomes (28) with a nominal beating frequency  $f$  on two swings, which can move freely in a plane (Fig. 1 and Figs. S1–S3). Oscillators within one population are coupled strongly by the motion of the swing onto which the metronomes are attached. As  $f$  is increased, more momentum is transferred to the swing, effectively leading to a stronger coupling among the metronomes. A single swing follows a phase transition from a disordered state to a synchronized state as the coupling within the population increases (28, 29). This mimics the synchronization of the gait of pedestrians on the Millennium Bridge (4) wobbling under the pedestrians’ feet. In our setup, emergent synchronization can be perceived both aurally (unison ticking) and visually (coherent motion of pendula). Finally, the weaker coupling between the two swings is achieved by tunable steel springs with an effective strength  $\kappa$ .

## Results

For nonzero spring coupling,  $\kappa > 0$ , we observe a **broad range of parameters in which chimeras** (Fig. 1C and Movie S1) and **further partially synchronized states emerge**. To explore this complex behavior quantitatively, we measure the metronomes’ oscillation phase  $\theta_k$ , their average frequencies  $\overline{\omega}_k$ , and the complex order parameter  $Z_p(t) = N^{-1} \sum_{k=1}^N e^{i[\theta_k^{(p)}(t) - \bar{\theta}_{\text{syn}}(t)]}$ , where  $p = 1, 2$  denotes the left or right population and  $\bar{\theta}_{\text{syn}}$  is the average phase of the synchronous population ( $|Z|$  quantifies the degree of synchronization:  $|Z| \approx 0$  for incoherent motion and  $|Z| \approx 1$  for synchronous motion).

Author contributions: E.A.M., S.T., and O.H. designed research; E.A.M., S.T., and A.F. performed research; E.A.M., S.T., and A.F. contributed new reagents/analytic tools; E.A.M. and S.T. analyzed data; E.A.M., S.T., A.F., and O.H. discussed the results and commented extensively on the manuscript at all stages of preparation; and E.A.M., S.T., and O.H. wrote the paper.

The authors declare no conflict of interest.

\*This Direct Submission article had a prearranged editor.

Freely available online through the PNAS open access option.

<sup>1</sup>E.A.M. and S.T. contributed equally to this work.

<sup>2</sup>To whom correspondence may be addressed. E-mail: erik.martens@ds.mpg.de or shashi@princeton.edu.

This article contains supporting information online at [www.pnas.org/lookup/suppl/doi:10.1073/pnas.1302880110/-DCSupplemental](http://www.pnas.org/lookup/suppl/doi:10.1073/pnas.1302880110/-DCSupplemental).



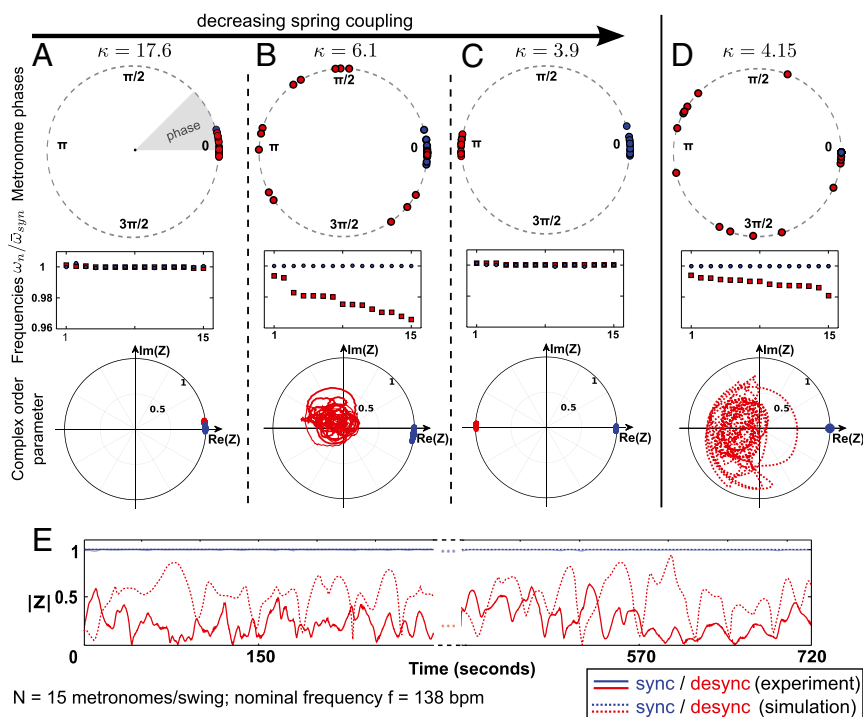


**Fig. 2.** Chimeras emerge with intermediate spring rate  $\kappa$  in a “competition” zone between two fully synchronous modes. With decreasing  $\kappa$ , we observe a transition from IP synchronization (A), over chimeras (B), to AP synchronization (C). The transition region also exhibits phase-clustered states and partial chimeras. (D and E) Simulations share all features of the experimental chimera. Data related to the synchronous and asynchronous populations are coded in blue and red, respectively. Angular frequencies are normalized with the average frequency of the synchronized population  $\bar{\omega}_{syn}$ . bpm, beats per minute.

$\tau = \omega t$ . In turn, the swings of length  $L$  are described as harmonic oscillators with eigenfrequency  $\Omega = \sqrt{g/L}$  and damping  $\mu_s$ . A swing is driven by the metronomes and the neighboring swing, to which it is coupled with a spring of strength  $\kappa$ :

$$\ddot{\Phi} + \Omega^2 \Phi - \kappa(\Psi - \Phi) + \mu_s \dot{\Phi} + \frac{x_0}{L} \sum_{k=1}^N \partial_{\tau\tau} \sin \phi_k = 0, \quad [2]$$

where terms (from left to right) are swing inertia, force of restitution, spring coupling, friction, and the inertia summed over

all metronomes on the same swing. Whereas  $\kappa$  determines the interpopulation coupling strength, the global coupling strength depends on the ratio of the metronome frequency and the swing eigenfrequency,  $(\omega/\Omega)^2$ . Using conditions similar to our experiments (but without frequency spread), chimeras obtained from simulations (Fig. 2 D and E) and the resulting phase diagram (Fig. 3 C) agree qualitatively very well with experiments (quantitative differences are likely due to the ad hoc metronome model and potential discrepancies in parametrization as discussed in *SI Text* and Fig. S6). Bistability of fully synchronized (SS) and symmetry-breaking (SD and DS) states is a

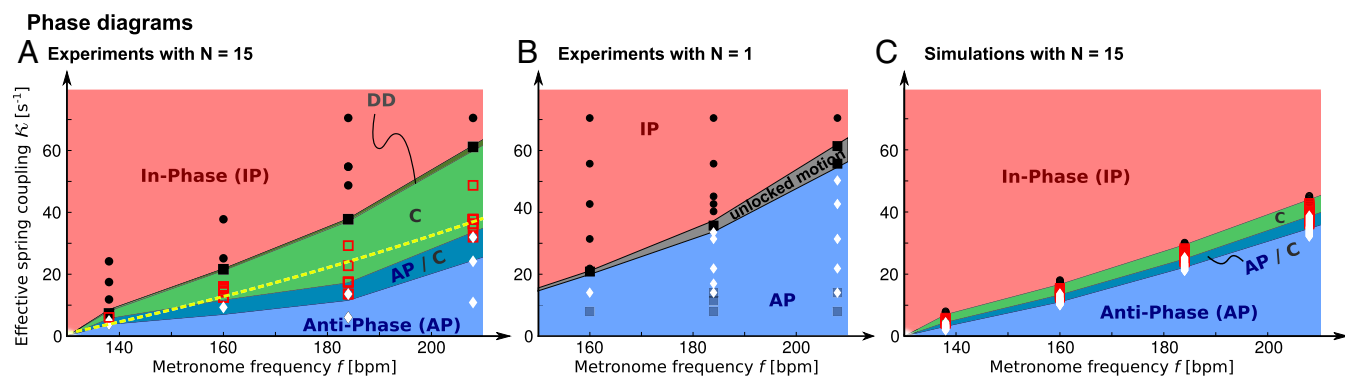


**Fig. 3.** Phase diagrams from experiments for  $N = 15$  (A) and  $N = 1$  (B) metronome(s) per swing and from numerical simulations with  $N = 15$  metronomes (C) with metronome frequency  $f$  vs. effective spring coupling  $\kappa = k/M(I/L)^2$ . IP (red) and AP (blue) synchronization modes surround the chimera parameter region C (green) and the bistable AP/C region with chimeras and AP synchronization. Symbols represent data points (color shadings are guides only). Region C, centered around the resonance curve of the swings' AP mode (yellow dashed line) defined by  $f \cdot \pi/60 = \sqrt{\Omega^2 + 2\kappa}$ , exhibits chimeras and other partially synchronized states. The bistable region AP/C exhibits chimera-like and synchronized AP states; DD represents a region where neither population synchronizes fully. For  $N = 1$ , we find a similar region of unlocked motion, where the metronomes never synchronize. The phase diagram from numerical simulations for identical metronomes exhibits the same qualitative structure as the experiment, except that the width of region C is smaller (*SI Text*). Parameter space in experiments and simulations was sampled with varying spring coupling  $\kappa$  for metronome frequencies  $f = 138, f = 160, f = 184$ , and  $f = 208$  bpm.



hallmark of the chimera instability (14), which is in distinct contrast to other symmetry-breaking scenarios mediated via supercritical transitions (13). It is therefore interesting to note that chimera states may coexist with AP synchronization modes in certain regions of the bifurcation diagram (Fig. 3A and C).

Notably, when metronomes on each swing synchronize in an IP or AP mode, one envisages that the swings, together with the attached metronomes, collectively behave like two “giant” metronomes. These modes correspond to excitations of the eigenmodes of the swing pair with frequencies  $\Omega$  (IP) and  $\sqrt{2\kappa + \Omega^2}$  (AP). Indeed, for  $N = 1$  metronome per swing (Fig. 1B), we find that due to momentum transfer, the swing strictly follows the motion of the attached metronome pendulum: The system behaves like Huygens’ experiment (i.e., with clocks replaced by metronomes). The metronomes settle into AP and IP synchronization modes for weak and strong coupling  $\kappa$ , respectively, as in modern reconstructions of Huygens’ setup (31). Additionally, we find a small region where unlocked motion is possible (Fig. 3B).

Generalizing Huygens’ experiment by adding internal degrees of freedom (i.e., metronomes) on each swing allows for much richer complex dynamics. A rich tapestry of complex states is uncovered (Fig. 4) in a transition from the AP to IP synchronization as the spring coupling  $\kappa$  is increased. In addition to chimeras, these include phase-clustered states (26): a “clustered chimera,” where oscillators are attracted to a clustered state but cannot quite attain frequency locking; a partial chimera, where the asynchronous population appears partially locked; and a quasiperiodic chimera (17, 18). The situation is aptly captured by the notion of “more is different” (32): Additional internal degrees of freedom open a door to unexpected complex behavior [i.e., unanticipated by mere extrapolation of simple collective behavior (32)]. Using Huygens’ term of the “odd sympathy of clocks” (1) to denote synchrony, the observed asymmetrical behavior might be described as an “antipathetic sympathy of clocks.”

Chimeras and other partly synchronous states emerge as a competition in an intermediate regime between IP and AP synchronization modes: As a result, both modes are destroyed, such that only one of the giant metronomes wins the tug-of-war and

remains synchronous, whereas the other one is broken apart. The resulting asymmetry is characterized by the domination of one giant over the other [i.e., the synchronous population forces the asynchronous population (33), acting like an energy sink]. Remarkably, we find that the parameter region with chimera-like behavior is centered around the resonance curve related to the swings’ antiphase eigenmode (Fig. 3A): Near resonance, the fabric of uniform synchronization is torn.

## Discussion

By devising a mechanical system composed of just two swings, a spring, and a number of metronomes (28), we have extended Huygens’ original experiment (1, 31) and demonstrated how chimeras emerge in the framework of classical mechanics. Recent experiments (26, 27) could only produce chimeras by exploiting sophisticated computer-controlled feedback, and the time delay of the coupling had to be carefully crafted in addition to tuning its strength; by contrast, in our realization, chimeras emerge generically using merely a spring, without any need to adjust parameters other than the coupling strength. Notably, our setup is composed of basic mechanical elements, such as inertia, friction, and spring rate, which have exact or generalized analogs in other areas, such as electronic (6, 34), optomechanical (35), chemical (7), and microbial systems or genetic circuits (36). The model we propose shows that the complex synchronization patterns found in the experiments are described by elementary dynamical processes that occur in diverse natural and technological settings. This raises the question of whether chimeras may have already been observed in such systems but remained unrecognized as such. For instance, our model equations translate directly to recent theoretical studies of synchronization in power grids (37–39) and optomechanical crystals (40, 41). Consequently, as power grid network topologies evolve to incorporate growing sources of renewable power, the resulting decentralized, hierarchical networks (37) may be threatened by chimera states, which could lead to large-scale partial blackouts and unexpected behavior. On the other hand, we envision that multistable patterns of synchrony and desynchrony (19) can be exploited to build on-chip memories

## Transition of chimera with increasing spring coupling

$N = 64$  metronomes per swing

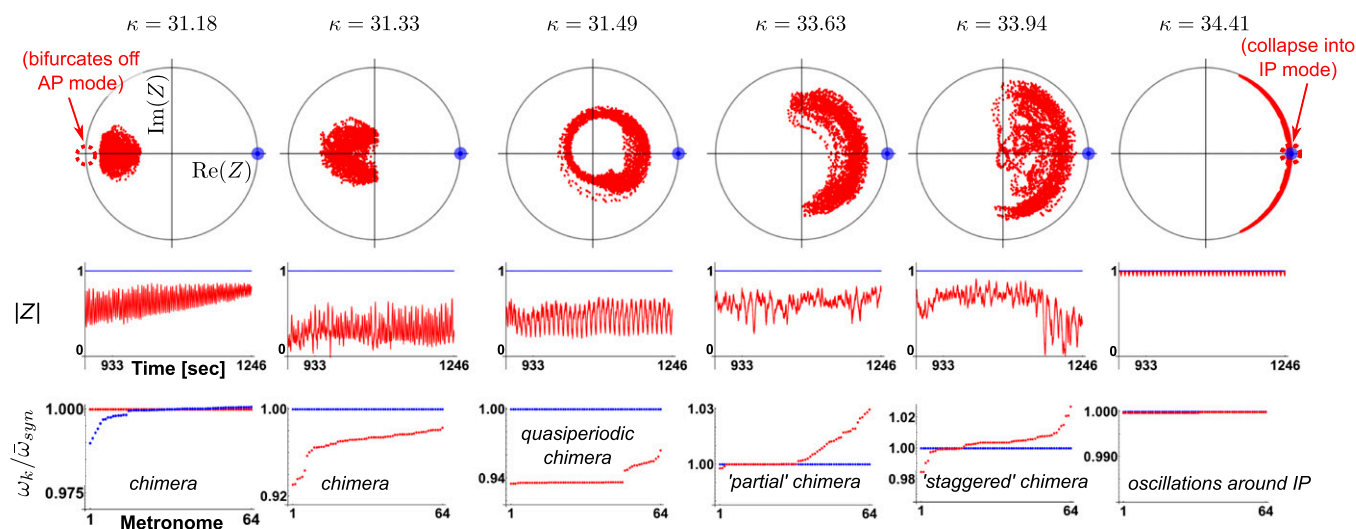


**Fig. 4.** Traversal of order parameter cloud with increasing spring coupling  $\kappa$ . A transition through a rich spectrum of chimera states becomes evident. Numerical simulations are carried out with  $N = 64$  metronomes (for parameters see *SI Text*). As  $\kappa$  increases, the complex order parameter  $Z_p$  bifurcates off from the AP mode at  $180^\circ$  and travels to the right, where it snaps into the IP synchronization mode at  $0^\circ$ . (Top) Complex order parameter  $Z$  is displayed. (Middle) Magnitude  $|Z_p|$  is displayed. (Bottom) Angular frequencies, normalized with the average frequency of the synchronized population  $\bar{\omega}_{syn}$ , are displayed. The synchronized population is shown in blue, and the desynchronized population is shown in red.

and computers based on arrays of micromechanical devices (35). We expect the physical mechanisms that we uncovered here will have important and far-reaching ramifications in the design and use of such technologies and in understanding chimera states in nature.

## Materials and Methods

**Experiments.** Two swings are suspended by four light hollow aluminum rods with a length of 50 cm (outer and inner diameters are 10 mm and 9 mm, respectively). The swings are attached to the rods via low-friction ball bearings to ensure smooth motion of the swings. The upper rod ends are attached in the same way on a large rigid support frame. The distance between the support frame and the board is set to  $L = 22$  cm. The motion of the two swings is constrained so that it can occur, to high precision, only in the x-y plane. Each swing is made of a 500-mm  $\times$  600-mm  $\times$  1-mm perforated aluminum plate. The total weight of each plate is  $915 \pm 4$  g. Each swing is loaded with  $N = 15$  metronomes with a weight of 94 g. The total weight of the swing and metronomes is  $M = 2.3$  kg. Two precision steel springs (Febrotec GmbH; spring constant  $k = 34$  N/m) are firmly attached with clamps to the two adjacent swing rods (Fig. 1A) at a distance  $l$  above the pivot point. Adjusting the spring lever  $l$  changes the effective spring strength  $\kappa = k/(l/L)^2$ . An experiment is started with a careful symmetry check of the system, by ensuring that the initial friction  $\mu_s$  is the same on

both swings. The metronome's nominal frequency is set to identical values  $\omega_n$ . We then connect the two swings with the spring firmly set at a distance  $l$  above the pivot points. The motion of the metronomes and the swings is video-recorded under UV illumination using a Nikon D90 camera mounted with an 18- to 55-mm DX format lens. Each experiment is repeated with inverted roles of the swings (i.e., a DS experiment is followed by an SD experiment), such that the left-to-right symmetry is checked thoroughly.

**Simulations.** Simulations were carried out with identical metronomes until a stationary state was reached (typically,  $\sim 2,000$  oscillation cycles). The phase diagram (Fig. 3C) was obtained by fixing the nominal metronome frequency  $f$  and then gradually increasing the effective spring rate  $\kappa$  (using similar parameters as in the experiment and  $N = 15$  metronomes per swing). For each parameter step, synchronous IP and AP states were continued quasiadiabatically, whereas simulations resulting in chimera-like states were reinitialized with randomized phases in one of the populations (SI Text).

**ACKNOWLEDGMENTS.** We thank H. Stone, S. Strogatz, K. Showalter, A. Pikovsky, M. Rosenblum, S. Herminghaus, and L. Goehring for useful comments, and H. J. Martens for valuable discussions on the experimental design. We express deep gratitude to Udo Krafft for his assistance with the experimental setup. This work was partly supported by a grant from the Human Frontier Science Program (to S.T.).

- Huygens C (1967) *Oeuvres complètes* (Swets & Zeitlinger Publishers, Amsterdam), Vol 15.
- Michaels DC, Matyas EP, Jalife J (1987) Mechanisms of sinoatrial pacemaker synchronization: A new hypothesis. *Circ Res* 61(5):704–714.
- Buck J, Buck E (1968) Mechanism of rhythmic synchronous flashing of fireflies. Fireflies of Southeast Asia may use anticipatory time-measuring in synchronizing their flashing. *Science* 159(3821):1319–1327.
- Strogatz SH, Abrams DM, McRobie A, Eckhardt B, Ott E (2005) Theoretical mechanics: Crowd synchrony on the Millennium Bridge. *Nature* 438(7064):43–44.
- Liu C, Weaver DR, Strogatz SH, Reppert SM (1997) Cellular construction of a circadian clock: Period determination in the suprachiasmatic nuclei. *Cell* 91(6):855–860.
- Wiesenfeld K, Colet P, Strogatz S (1998) Frequency locking in Josephson arrays: Connection with the Kuramoto model. *Phys Rev E Stat Phys Plasmas Fluids Relat Interdiscip Topics* 57(2):1563–1569.
- Kiss IZ, Zhai Y, Hudson JL (2002) Emerging coherence in a population of chemical oscillators. *Science* 296(5573):1676–1678.
- Taylor AF, Tinsley MR, Wang F, Huang Z, Showalter K (2009) Dynamical quorum sensing and synchronization in large populations of chemical oscillators. *Science* 323(5914):614–617.
- Dano S, Sørensen PG, Hynne F (1999) Sustained oscillations in living cells. *Nature* 402(6759):320–322.
- Massie TM, Blasius B, Weithoff G, Gaedke U, Fussmann GF (2010) Cycles, phase synchronization, and entrainment in single-species phytoplankton populations. *Proc Natl Acad Sci USA* 107(9):4236–4241.
- Motter AE (2010) Spontaneous synchrony breaking. *Nat Phys* 6(3):164–165.
- Kuramoto Y, Battogtokh D (2002) Coexistence of coherence and incoherence in nonlocally coupled phase oscillators. *Nonlinear Phenomena in Complex Systems* 5(4):380–385.
- Abrams DM, Strogatz SH (2004) Chimera states for coupled oscillators. *Phys Rev Lett* 93(17):174102.
- Abrams DM, Mirollo R, Strogatz SH, Wiley DA (2008) Solvable model for chimera states of coupled oscillators. *Phys Rev Lett* 101(8):084103.
- Montbrió E, Kurths J, Blasius B (2004) Synchronization of two interacting populations of oscillators. *Phys Rev E Stat Nonlin Soft Matter Phys* 70(5 Pt 2):056125.
- Omel'chenko OE, Maistrenko YL, Tass PA (2008) Chimera states: The natural link between coherence and incoherence. *Phys Rev Lett* 100(4):044105.
- Pikovsky A, Rosenblum M (2008) Partially integrable dynamics of hierarchical populations of coupled oscillators. *Phys Rev Lett* 101(26):264103.
- Bordyugov G, Pikovsky A, Rosenblum M (2010) Self-emerging and turbulent chimeras in oscillator chains. *Phys Rev E Stat Nonlin Soft Matter Phys* 82(3 Pt 2):035205.
- Martens EA (2010) Bistable chimera attractors on a triangular network of oscillator populations. *Phys Rev E Stat Nonlin Soft Matter Phys* 82(1 Pt 2):016216.
- Martens EA, Laing CR, Strogatz SH (2010) Solvable model of spiral wave chimeras. *Phys Rev Lett* 104(4):044101.
- Laing CR (2009) The dynamics of chimera states in heterogeneous Kuramoto networks. *Physica D* 238(16):1569–1588.
- Laing CR, Rajendran K, Kevrekidis IG (2012) Chimeras in random non-complete networks of phase oscillators. *Chaos: An interdisciplinary Journal of Nonlinear Science* 22(1):013132.
- Olmi S, Politi A, Torcini A (2010) Collective chaos in pulse-coupled neural networks. *Europhys Lett* 92(6):60007.
- Phillips JR, White J, Orlando TP, Orlando TP, van der Zant HS (1993) Influence of induced magnetic fields on the static properties of Josephson-junction arrays. *Phys Rev B Condens Matter* 47(9):5219–5229.
- Swindale NV (1980) A model for the formation of ocular dominance stripes. *Proc R Soc Lond B Biol Sci* 208(1171):243–264.
- Tinsley MR, Nkomo S, Showalter K (2012) Chimera and phase-cluster states in populations of coupled chemical oscillators. *Nat Phys* 8(8):662–665.
- Hagerstrom AM, et al. (2012) Experimental observation of chimeras in coupled-map lattices. *Nat Phys* 8(8):658–661.
- Pantaleone J (2002) Synchronization of metronomes. *Am J Phys* 70(10):992–1000.
- Ulrichs H, Mann A, Parlitz U (2009) Synchronization and chaotic dynamics of coupled mechanical metronomes. *Chaos* 19(4):043120.
- Golomb D, Hansel D, Shraiman B, Sompolsky H (1992) Clustering in globally coupled phase oscillators. *Phys Rev A* 45(6):3516–3530.
- Bennett M, Schatz M, Wiesenfeld K (2002) Huygen's clocks. *Proc R Soc Lond A Math Phys Sci* 458(2019):563–579.
- Anderson PW (1972) More is different. *Science* 177(4047):393–396.
- Childs LM, Strogatz SH (2008) Stability diagram for the forced Kuramoto model. *Chaos* 18(4):043128.
- Temirbayev A, Zhanabaev Z, Tarasov S, Ponomarenko V, Rosenblum M (2012) Experiments on oscillator ensembles with global nonlinear coupling. *Phys Rev E Stat Nonlin Soft Matter Phys* 85(1 Pt 2):015204.
- Zhang M, et al. (2012) Synchronization of micromechanical oscillators using light. *Phys Rev Lett* 109(23):233906.
- Danino T, Mondragón-Palomino O, Tsimring L, Hasty J (2010) A synchronized quorum of genetic clocks. *Nature* 463(7279):326–330.
- Rohden M, Sorge A, Timme M, Witthaut D (2012) Self-organized synchronization in decentralized power grids. *Phys Rev Lett* 109(6):064101.
- Dörfler F, Chertkov M, Bullo F (2013) Synchronization in complex oscillator networks and smart grids. *Proc Natl Acad Sci USA* 110(6):2005–2010.
- Motter AE, Myers SA, Anghel M, Nishikawa T (2013) Spontaneous synchrony in power-grid networks. *Nat Phys* 9(1):191–197.
- Eichenfield M, Chan J, Camacho RM, Vahala KJ, Painter O (2009) Optomechanical crystals. *Nature* 462(7269):78–82.
- Heinrich GH, Ludwig M, Qian J, Kubala B, Marquardt F (2011) Collective dynamics in optomechanical arrays. *Phys Rev Lett* 107(4):043603.

# Supporting Information

Martens et al. 10.1073/pnas.1302880110

## SI Text

### Experimental Setup

**Swing.** We briefly describe the experimental setup shown in Fig. S1. Two swings are suspended by four light hollow aluminum rods with a length of 50 cm (outer and inner diameters are 10 mm and 9 mm, respectively). The swings are attached to the rods via low-friction ball bearings to ensure smooth motion of the swings. The upper ends of the rods are attached in the same way on a large rigid support frame. The distance between the support frame and the board is set to  $L = 22$  cm. The motion of the two swings ( $A$  and  $B$ ) is constrained so that it (to high precision) can only occur in the  $(x, y)$  plane along the arc lengths  $S_A = L\Psi$  and  $S_B = L\Phi$ , respectively. Each swing is made of a 500-mm  $\times$  600-mm  $\times$  1-mm perforated aluminum plate. To make the plates stiff and flat, they are bent at the edges, and aluminum tubes of square cross-section are placed underneath the board for further support. The total mass of each plate is  $m_s = 915 \pm 4$  g.

Each swing is loaded with  $N = 15$  metronomes of mass  $m_m = m + m_{\text{box}} = 93$  g, where  $m = 28$  g is the mass of the entire metronome pendulum (composed of a larger rigid part,  $m_p = 23$  g, and a smaller adjustable bob,  $m_{\text{bob}} = 5$  g, to set the frequency);  $m_{\text{box}} = 65$  g is the mass of the metronome's box (Fig. S3). Thus, the total mass of swing and metronomes amounts to  $M = m_s + N \times m_m \approx 2.3$  kg.

The adjacent swing rods (two pairs at the front and back sides of the swing) are connected with two precision metallic springs (the back pair of rods is shown in Fig. S24). The pivots of two adjacent rods are set to a distance of  $L_p = 20$  cm. The springs used in our study (Febrotec GmbH) have the following characteristics: outside diameter of 6.14 mm, wire diameter of 0.46 mm, unloaded length of 38.1 mm, preload force of 0.41 N, and force at a length of 152.2 mm = 4.37 N. For a single spring, we measured a rate of  $34 \text{ N} \cdot \text{m}^{-1}$  (Fig. S2B); thus, the total spring rate yielded by the two springs used in our setup is  $k = 68 \text{ N} \cdot \text{m}^{-1}$ . Both springs are attached to plastic clamps at both ends (Fig. S24); the clamps are firmly attached to the rods at distance  $l$  above the pivot point. The clamps can be slid up and down while still being firmly fixed to the rods during an experiment. Thereby, we change the spring lever  $l$  and the associated torque (i.e., we effectively tune the spring coupling strength).

**Swing equilibrium angle.** The swing positions  $\Phi, \Psi$  can be parametrized with small-amplitude variations  $\Phi', \Psi'$  around their equilibrium angles  $\Phi^*, \Psi^*$ ; that is:

$$\Phi'(t) = \Phi(t) - \Phi^*, \quad [\text{S1}]$$

$$\Psi'(t) = \Psi(t) - \Psi^*, \quad [\text{S2}]$$

for which the equilibrium angles are  $\sim 1^\circ \dots 2^\circ$ . Typical equilibrium angles with varying spring leverage  $l$  are summarized in Table S1; their magnitude is small, which allows us to make the small-angle approximations described below. The equilibrium torque balance defines an equilibrium spring force,  $\tilde{F}_s^*$ :

$$l \tilde{F}_s^* = -L Mg \sin \Phi^*. \quad [\text{S3}]$$

Note that  $\Psi^* = -\Phi^* < 0$  due to the symmetry of the setup.

**Swing friction.** To estimate the friction coefficient in the swing on an experimental basis, we observe the equation of motion for one swing:

$$\partial_t^2 \Phi = -\frac{g}{L} \sin \Phi - \frac{\nu_s}{M} \partial_t \Phi. \quad [\text{S4}]$$

The eigenfrequency of the swing is  $\Omega = \sqrt{g/L} \approx 6.67 \text{ rad} \cdot \text{s}^{-1}$ . For small angles  $\sin \Phi \approx \Phi$ , we obtain the solution

$$L \Phi(t) = L \Phi_0 e^{-\nu_s t/(2M)} \cos \left[ \sqrt{\Omega^2 - (\nu_s/4M)^2} t \right]. \quad [\text{S5}]$$

We infer the friction coefficient  $\nu_s$  by measuring the evolution of the amplitude of the swing  $L \Phi(t)$ , initially removed from its equilibrium position by an angle  $\Phi(0) = \Phi_0$  and released without any celerity,  $\partial_t \Phi(0) = 0$ . By observing the decaying amplitude  $L \Phi(t)$  over a few minutes and comparing the data with Eq. S5, we find that, typically,  $\bar{\nu}_s \sim 0.1 \text{ kg/s}$ .

**Metronome.** The working principle behind the metronome mechanism is identical to Huygens' pendulum clocks (1), except that the escapement in the metronome is driven by a spring rather than a mass pulled by gravity. Although friction inherent to the mechanical elements attenuates large-amplitude oscillations toward the nominal metronome oscillation amplitude, small pendulum oscillations are amplified by the spring energy feeding the pendulum via the escapement mechanism. Together, this gives the metronome the characteristics of a self-sustained oscillator (2).

In our experiment, we use Wittner Taktell Supermini metronomes as utilized in previous studies (2), covering a frequency range of 40 (largo) to 208 (prestissimo) beats per minute (bpm), with a standard deviation of relative frequencies of  $\sim 1\%$ . Each metronome has physical dimensions of 30 mm  $\times$  37 mm  $\times$  104 mm and mass  $m_m = 93$  g. When fully wound up, each metronome ticks for a duration of  $\sim 20$  min (depending on the adjusted frequency  $f$ ), corresponding to  $\sim 1,500$  oscillation cycles.

During operation, each metronome is firmly attached on the swing plate with double-sided Scotch tape; the standard position of each metronome is marked with a pen on the swing boards, such that we maintain the same arrangement of metronomes on the plate for each experiment. The total mass of the swing is  $M = m_s + N \times m_m = 2.3 \text{ kg}$ . To record the angle displacement of each metronome,  $\phi_i$  and  $\psi_i$ , from the swings A and B, respectively, small round stickers with a diameter of  $\sim 10$  mm are attached at the upper part of the rod. The stickers are UV fluorescent, which allows digital tracking of the metronome motion. We verified that their addition (negligible mass) does not change the metronome characteristics relevant to the observations made here.

The metronome may be conceptually split into two parts: (i) the rigid, nonmoving box of mass  $m_{\text{box}}$  containing the spring and escapement mechanism driving the pendulum and (ii) the oscillating pendulum of mass  $m_p$ . It is composed of a rod with a weight attached on the lower end (the counterweight); on the top end, there is a second weight (bob) that can be moved up and down (Fig. S3).

**Frequency.** The only control parameter of the metronome is its beating frequency. It is adjusted by sliding the bob up and down, thereby altering the first (center mass,  $r_{\text{cm}}$ ) and second moments of the metronome pendulum,  $I$ .

The (quasi-)linear eigenfrequency  $\omega$  of the metronome (Eqs. S31 and S32) is not exactly equal to the nominal frequency  $f$  of the nonlinear oscillator. The relationship between the two frequencies can be estimated by considering higher order expansions of the sine term and the van der Pol term in the governing Eq. S28. A first-order estimate of the nominal frequency is given by (2, 3)



$$\omega_n \approx \left[ 1 - \left( \frac{\theta_0}{2} \right)^2 \right] \omega. \quad [\text{S6}]$$

The angular frequencies  $\omega$  and  $\omega_n$  are measured in radians per second rather than in beats per minute. The conversion between the two units is given via  $\omega = f \cdot \pi/60$  (two beats correspond to one oscillation period). Half of the standard displacement angle of the pendulum is expressed as  $\theta_0 \approx 19^\circ$  (see model below).

**Center mass and second moment of inertia.** The first and second moments of inertia enter as parameters in the model that we develop further below. We need to determine the relationship between these moments and the metronome frequency  $f$ , which we use as an experimental control parameter. Determining the two moments by disassembling the pendulum into separate parts (bob, pendulum rod, counterweight, axle, and axle-to-rod connector) and measuring their mass and relative positions result in a tedious estimation exercise, which is prone to undue error. [To achieve accurate nominal frequencies, the bobs are manually calibrated (i.e., the manufacturer filed each pendulum bob individually to fit, reflecting the high sensitivity on small mass and geometric variations)]. We therefore resort to a simple parameter fit, based on first principles and few empirical measurements. We measure all distances relative to the pivot, such that positions on the upper part of the pendulum rod are positive. Let us denote  $l_{\text{bob}}$  as the distance of the bob to the pivot (axle) of the metronome (the bob's center mass is located about 5 mm below its upper edge). The center mass of the pendulum is then located at  $r_{\text{cm}} = (m_0 l_0 + m_{\text{bob}} l_{\text{bob}}) / m = r_0 + m_{\text{bob}} / m \cdot l_{\text{bob}}$ , and the second moment of inertia is  $I = m_0 l_0^2 + m_{\text{bob}} l_{\text{bob}}^2 = I_0 + m_{\text{bob}} l_{\text{bob}}^2$ . The mass of the bob is  $m_{\text{bob}} = 5$  g, and the mass of the entire pendulum is  $m = 28$  g. To determine  $r_0$ , we detach the pendulum from its box and set the bob to the maximum position at  $l_{\text{bob}} \approx 26$  mm at frequency  $f = 208$  bpm. We then balance the pendulum on the edge of a razor blade and find that  $r_{\text{cm}} \approx -7.5$  mm, corresponding to  $r_0 = -12.1$  mm. We thus have the (by definition) positive center mass distance:

$$r_{\text{cm}} \approx |-0.0121 \text{ m} + 0.178 \cdot l_{\text{bob}} [\text{m}]| > 0. \quad [\text{S7}]$$

The second moment of inertia is related to the quasilinear eigenfrequency  $\omega$  via Eq. S33,  $I = mg r_{\text{cm}} \omega^{-2}$ , which we evaluate for  $f = 208$  bpm by using the above approximation for  $r_{\text{cm}}$  and Eq. S10 below:

$$I_0 = I|_{f=208} - m_{\text{bob}} l_{\text{bob}}^2 = 1.29 \times 10^{-5} \text{ kg} \cdot \text{m}^2. \quad [\text{S8}]$$

We then have

$$I = 1.29 \times 10^{-5} \text{ kg} \cdot \text{m}^2 + 5 \times 10^{-3} \text{ kg} \cdot l_{\text{bob}}^2 [\text{m}^2]. \quad [\text{S9}]$$

Finally, by simply reading off values for  $l_{\text{bob}}$  for given nominal frequencies  $f$ , we find the following linear fit:

$$l_{\text{bob}} \approx 7.3 \times 10^{-2} \text{ m} - 2.2 \times 10^{-4} \text{ m/bpm} \times f [\text{bpm}], \quad [\text{S10}]$$

which turns out to be approximately linear for the frequency range considered. Combination of Eqs. S7–S10 yields the required relationship for  $I = I(f)$  and  $r_{\text{cm}} = r_{\text{cm}}(f)$ .

## Experimental Methods

**Experimental Protocol.** An experiment is started with a careful symmetry check of the system: The two uncoupled boards are displaced from their equilibrium position (in the uncoupled case, at equilibrium, the rods are vertical:  $\Phi^* = \Psi^* = 0$ ) and released at the same time. By observing the decrease of amplitude  $L\Phi(t)$  and

$L\Psi(t)$ , we check that the initial friction  $\nu_s$  is the same on both swings. All the metronomes are then wound up, and their nominal frequency  $\omega_n$  is adjusted to the same value and double-checked. The metronomes are then firmly and precisely placed on each board. We then connect the two swings with the spring, which is firmly set at a distance  $l$  above the pivot points. The metronomes are put in motion. The initial conditions are prepared to be compliant to one of two states: (i) desync-sync (DS) [equivalently, sync-desync (SD)] corresponding to desynchrony and synchrony on the left or right swing, respectively, or (ii) both populations are started in desynchrony (desync-desync). The desynchrony of the population on one swing is ensured by blocking the motion of the swing physically; meanwhile, the other population on the other swing achieves full synchrony via its free swing motion. The start of an experiment is then marked by the time point when this swing is released. The motion of the metronomes and the swings is recorded by video-recording under UV illumination using a Nikon D90 camera mounted with an 18- to 55-mm lens (DX format). After the experiment, we repeat the protocol for the very same parameters and invert the roles of the swings (i.e., a DS experiment is followed by an SD experiment), such that the left-to-right symmetry is checked thoroughly.

**Data Analysis.** The videos from the experiment are further processed to extract quantitative information by image processing using MATLAB (MathWorks). The metronome pendula and the swings are marked by UV fluorescent spots (Fig. S1B). These bright spots show up as circular white regions in the images, which are then tracked by their centroids to obtain the positions  $x(t)$  and  $y(t)$  of the metronome pendula as a function of time. The phases  $\theta_k^{(1)}(t)$  and  $\theta_k^{(2)}(t)$  of the metronomes and  $\Theta^{(1)}(t)$  and  $\Theta^{(2)}(t)$  of the swing oscillations on populations 1 and 2, respectively, are obtained from the time tracks of those positions using the Hilbert transform in MATLAB [this technique works well because the signal is sufficiently narrow-banded (4, 5):

$$H \left[ x_k^{(p)}(t) - X^{(p)}(t) - \left\langle x_k^{(p)}(t) - X^{(p)}(t) \right\rangle_t \right] \\ = \pi^{-1} \int_{-\infty}^{\infty} \left[ x_k^{(p)}(t') - X^{(p)}(t') - \left\langle x_k^{(p)}(t') - X^{(p)}(t') \right\rangle_t \right] / (t - t') dt', \quad [\text{S11}]$$

where  $x_k^{(p)}(t)$  is the position of the  $k$ th metronome bob on swing  $p = 1, 2$ ,  $X^{(p)}(t)$  is the position of the swing on which the metronome is attached, and  $\langle x_k^{(p)}(t) - X^{(p)}(t) \rangle_t$  is its temporal mean, which we subtract from the signal to center the data around the origin. The Hilbert transform allows us to reconstruct the analytical representation of the signal  $x(t)$  [i.e.,  $x_a(t) = x(t) + iH(x)(t)$ ]; for a narrow-banded signal, we then have  $x_a(t) = A(t)e^{i[\omega t + \theta(t)]}$ . The phases  $\theta_k(t)$  are used to calculate time-averaged frequencies and to quantify the synchronization using the Kuramoto order parameters for populations  $p = 1, 2$ :

$$Z_p(t) \equiv \frac{1}{N} \sum_{k=1}^N \exp \left\{ i \left[ \theta_k^{(p)}(t) - \bar{\theta}_{\text{syn}}^{(p)}(t) \right] \right\}, \quad [\text{S12}]$$

where  $\bar{\theta}_{\text{syn}}(t)$  is the average phase of the synchronous population at time  $t$ . Further, the phases are used to obtain the average frequencies over a time window  $T$  [i.e.,  $\bar{\omega}_k \approx [\phi_k(T) - \phi_k(0)]/T$ ]. These frequencies may be compared with the average frequency of the synchronous population,  $\bar{\omega}_{\text{syn}} \equiv N^{-1} \sum_{k=1}^N \bar{\omega}_k$ .

## Further Experimental Results

In addition to the chimera behavior, we find other collective modes. For instance, a phase-clustered state is shown in Fig. S4.

The relative frequencies of the synchronized and desynchronized populations reveal the presence of distinct frequency clusters in the desynchronized population. A snapshot of the metronome phase for the synchronized population,  $S$ , and the desynchronized population further reveals the existence of four phase clusters,  $C_1$ ,  $C_2$ ,  $C_3$ , and  $C_4$ , within the desynchronized population. To analyze these clusters in more detail, we calculate the order parameter  $Z(t)$  for each of the clusters individually. Although cluster  $C_1$  is locked in antiphase with  $S$ , clusters  $C_2$ ,  $C_3$ , and  $C_4$  are not phase-locked with respect to  $S$ . However, clusters  $C_3$  and  $C_4$  are locked roughly in antiphase with each other, although still drifting with respect to  $S$ . It is remarkable to note that these various complex dynamics within the desynchronized population all together give rise to a time-varying order parameter, which, after an initial transient, appears highly periodic.

All experimental states have been examined in the manner outlined above; in particular, for the chimera states, we have ensured that phase locking between any of the individual oscillators within the asynchronous population is absent.

### Model

The dynamics of the two swings are described by the angles  $\Phi(t)$  and  $\Psi(t)$  and their corresponding angular velocities (Figs. S1 and S5), which describe the motion along arc coordinates  $S_A = L\Phi$  and  $S_B = L\Psi$ . The motion of the metronome pendula is described by their displacement angles  $\phi_i(t)$  on swing  $A$  and  $\psi_i(t)$  on swing  $B$ , respectively. As explained above, to set up the governing equations, we conceptually divide the system into two subsystems: (i) the system of the two coupled swings and (ii) the system of the  $N$  metronomes populating each swing. For all angles, we use mathematically positive orientation (Figs. S1 and S3).

**Swing System.** We derive equations of motion for the two swings by considering the external forces acting on the center mass system of swing  $A$  (and swing  $B$ , respectively):

$$M \partial_t^2 \begin{pmatrix} X_{\text{cm}}^A \\ Y_{\text{cm}}^A \end{pmatrix} = \mathbf{F}_{\text{ext}}^A. \quad [\text{S13}]$$

The center mass system is composed of the swing board of mass  $m_s$  and the metronomes of mass  $m_m$  [i.e.,  $M = m_s + N \cdot m_m = m_s + N(m_{\text{box}} + m_p)$ ]. The masses of the suspension rods are negligible in comparison to the mass of the swings and the metronomes  $M$ . The external force acting on the center mass system is composed of the sum  $\mathbf{F}_{\text{ext}}^A = \mathbf{F}_g^A + \mathbf{F}_s^A + \mathbf{F}_\nu^A + \mathbf{F}_{\text{rod}}^A$  [i.e., the sum of the following forces (Fig. S5)]:

i) Gravity:

$$\mathbf{F}_g^A = -Mg \hat{\mathbf{e}}_y. \quad [\text{S14}]$$

ii) Spring force:

$$\mathbf{F}_s^A = -\frac{l}{L} \tilde{\mathbf{F}}_s^A = -\frac{l}{L} \left[ \tilde{F}_s^* + kl(\Phi' - \Psi') \right] \hat{\mathbf{e}}_x, \quad [\text{S15}]$$

where  $\Phi'$ ,  $\Psi'$  are the displacement angles measured from the equilibrium and  $\tilde{F}_s^*$  is the equilibrium spring force defined in Eq. S3.

iii) Friction: The swing friction force is given by

$$\mathbf{F}_\nu^A = -\nu_s \partial_t S_A \hat{\mathbf{e}}_s = -\nu_s L \partial_t \Phi \hat{\mathbf{e}}_s, \quad [\text{S16}]$$

where we introduce the unit vector  $\hat{\mathbf{e}}_s = (\cos \Phi, \sin \Phi)$ .

iv) Rod force: The force exerted by the pendulum rods that constrain the motion is

$$\mathbf{F}_{\text{rod}} = \left[ -(\mathbf{F}_g^A + \mathbf{F}_s^A + \mathbf{F}_\nu^A) \cdot \hat{\mathbf{e}}_r \right] \hat{\mathbf{e}}_r, \quad [\text{S17}]$$

where we introduce the unit vector  $\hat{\mathbf{e}}_r = (\sin \Phi, -\cos \Phi)$  perpendicular to  $\hat{\mathbf{e}}_s$  (this force cancels later).

**Center mass system.** The  $X$ -component of the center mass location of swing  $A$  is given by

$$MX_{\text{cm}}^A = (m_s + Nm_{\text{box}})X^A + m \sum_{j=1}^N (X^A + x_j^A) = MX^A + m \sum_{j=1}^N x_j^A,$$

where  $X^A \equiv L \sin \Phi$  and  $X^B \equiv L_p + L \sin \Psi$  are the positions of swings  $A$  and  $B$ , respectively; here, we have merged the masses of the rigid parts of the metronome mass (i.e., the box) with that of the swing,  $m_s$ . The center mass of each pendulum  $k$  is relative to swing  $A$  located at

$$x_j^A = a_k + r_{\text{cm}} \sin \phi_j, \quad [\text{S18}]$$

where  $a_k$  are the positions of metronome  $k$  on the swing board,  $r_{\text{cm}}$  is the distance of the center mass of the pendulum relative to its pivot, and  $\phi_k$  is the angle of metronome  $k$  on swing  $A$  with the vertical axis (Fig. S3). This allows us to express the inertia of the swing's center mass system in terms of the swing coordinate and the metronome coordinates  $x_k$ . We thus have

$$M \partial_t^2 X_{\text{cm}}^A = M \partial_t^2 X^A + m \sum_{j=1}^N \partial_t^2 x_j^A. \quad [\text{S19}]$$

Because all metronomes are firmly attached to the swing (i.e.,  $\partial_t a_k = 0$ ), we obtain

$$M \partial_t^2 X_{\text{cm}}^A = M \partial_t^2 X^A + mr_{\text{cm}} \sum_{j=1}^N \partial_t^2 \sin \phi_j, \quad [\text{S20}]$$

$$M \partial_t^2 Y_{\text{cm}}^A = M \partial_t^2 Y^A + mr_{\text{cm}} \sum_{j=1}^N \partial_t^2 \cos \phi_j, \quad [\text{S21}]$$

where the latter is the analogous expression for the center mass position in the  $Y$ -direction.

Projection of the force balance (Eq. S13) onto  $\hat{\mathbf{e}}_s$  yields

$$\begin{aligned} & ML (\cos \Phi \partial_t^2 \sin \Phi + \sin \Phi \partial_t^2 \cos \Phi) \\ & + mr_{\text{cm}} \sum_{j=1}^N (\cos \Phi \partial_{tt} \sin \phi_j + \sin \Phi \partial_{tt} \cos \phi_j) \\ & = -Mg \sin \Phi - \frac{l}{L} \left[ \tilde{F}_s^* + kl(\Phi' - \Psi') \right] \cos \Phi - \nu_s L \partial_t \Phi. \end{aligned} \quad [\text{S22}]$$

**Small-angle approximation.** The displacements  $\Phi$ ,  $\Psi$  of the two swings are small; in particular, the swings make small-amplitude oscillations ( $\sim 1^\circ$  to  $2^\circ$ ) around their equilibrium positions  $\Phi^*$  and  $\Psi^*$  in Eq. S1; that is:

$$\Phi(t) = \Phi^* + \Phi'(t),$$



$$\Psi(t) = \Psi^* + \Psi'(t).$$

In our experiments, the equilibrium angles lie in a range from  $5^\circ$  to  $10^\circ$  (Table S1). In the following, we shall therefore use the small-angle approximations  $\sin \Phi = \Phi + \mathcal{O}(\Phi^3)$  and  $\cos \Phi = 1 + \mathcal{O}(\Phi^2)$ . The approximated dynamics are then given by

$$\begin{aligned} ML\partial_t^2\Phi + mr_{\text{cm}} \sum_{j=1}^N (\partial_{tt} \sin \phi_j + \Phi \partial_{tt} \cos \phi_j) \\ = -Mg\Phi - \frac{l}{L} \left[ \tilde{F}_s^* + kl(\Phi' - \Psi') \right] - \nu_s L \partial_t \Phi. \end{aligned} \quad [\text{S23}]$$

Further, we simplify the equation by observing that  $\left| \sum_{j=1}^N \partial_{tt} \sin \phi_j \right| \gg \left| \Phi \cdot \sum_{j=1}^N \partial_{tt} \cos \phi_j \right| \sim |\Phi|$  and by parameterizing the swing angles in terms of their equilibrium angles (Eq. S1):

$$\begin{aligned} ML\partial_t^2\Phi' + mr_{\text{cm}} \sum_{j=1}^N \partial_{tt} \sin \phi_j \\ = -Mg(\Phi^* + \Phi') - \frac{l}{L} \left[ \tilde{F}_s^* + kl(\Phi' - \Psi') \right] - \nu_s L \partial_t \Phi'. \end{aligned} \quad [\text{S24}]$$

Cancellation of the swing equilibrium force  $\tilde{F}_s^*$  in Eq. S3 and noting that  $\Psi^* = -\Phi^* > 0$  yields the governing equations for swings  $A$  and  $B$ :

$$\partial_t^2\Phi' = -\frac{g}{L}\Phi' + \frac{k}{ML^2}(\Psi' - \Phi') - \frac{\nu_s}{M}\partial_t\Phi' - \frac{m}{ML}r_{\text{cm}} \sum_{j=1}^N \partial_t^2 \sin \phi_j, \quad [\text{S25}]$$

$$\partial_t^2\Psi' = -\frac{g}{L}\Psi' + \frac{k}{ML^2}(\Phi' - \Psi') - \frac{\nu_s}{M}\partial_t\Psi' - \frac{m}{ML}r_{\text{cm}} \sum_{j=1}^N \partial_t^2 \sin \psi_j. \quad [\text{S26}]$$

**Metronome System.** To close Eqs. S25 and S26, we need to describe the motion of the angles of the pendula on swings  $A$  and  $B$ . The pendulum angles with the vertical are denoted by  $\phi_i$  and  $\psi_i$  for populations on swings  $A$  and  $B$ , respectively (Fig. S3). We have

$$\begin{aligned} 0 = I \partial_t^2 \phi_i + mg r_{\text{cm}} \sin \phi_i + \nu_m \partial_t \phi_i \left[ \left( \frac{\phi_i}{\theta_0} \right)^2 - 1 \right] \\ + mr_{\text{cm}} \cos \phi_i \partial_t^2 X^A, \end{aligned} \quad [\text{S27}]$$

and the analogous equations for  $\psi_i$ . The first term is the rotational inertia with the second moment  $I = \int \rho(r)r^2 dV$ , and the second term is due to gravity with the first moment  $r_{\text{cm}}$  of the metronome pendulum. The two moments  $r_{\text{cm}}$  and  $I$  are parameterized in terms of the metronome frequency  $f$  (Eqs. S7, S9, and S10). The third term is a van der Pol term that is commonly used in literature to model the escapement mechanism [e.g., refs. 1, 6, 7 or the study by Pantaleone (2), who uses the same make of metronomes as we do here]. The van der Pol term is parameterized with two parameters  $\nu_m$  and  $\theta_0$ . The standard displacement angle of an uncoupled, nonaccelerated metronome pendulum ( $2\theta_0 = 37^\circ - 38^\circ$ ) mounted on a horizontal surface is  $2\theta_0$ . The resulting dissipation is amplitude-dependent and switches sign depending on the magnitude of the metronome's displacement angle: When the pendulum displacement  $\phi_i > \theta_0$ , energy is dissipated, whereas in the opposite case, the motion of the pendulum

is amplified (escapement mechanism transfers spring energy to the pendulum); in effect, the oscillation assumes a limit cycle oscillation. Even though the term is ad hoc, it is (qualitatively) generic in the sense that it may be considered a symmetrical expansion of a dissipation term of the type  $\partial_t \phi \cdot f(\phi)$  to second order in  $\phi$ , where  $f(\phi)$  must be symmetrical [note, however, that the tilting of a metronome, such that it is not standing vertically, results in asymmetrical ticking (long-short-long-...)]. The van der Pol term may also be thought of as a time-average proxy of the discrete process performed by the escapement.

Finally, the last term comes from the inertia exerted from the center mass swing motion. The torque is computed via the projection of the swing motion in  $X$ -direction into the arc coordinates, (i.e.,  $m r_{\text{cm}} \cos \phi_i \partial_t^2 X$ ). The center mass of swing  $A$  is

$$M X^A = M L \sin \Phi = ML(\Phi^* + \Phi') + \mathcal{O}(\Phi^3).$$

Thus, neglecting higher order terms, we have  $\partial_t^2 X^A \approx L \partial_t^2 \Phi'$ , and we get

$$\partial_t^2 \phi_i = -\frac{m}{I} g r_{\text{cm}} \sin \phi_i - \frac{\nu_m}{I} \partial_t \phi_i \left[ \left( \frac{\phi_i}{\theta_0} \right)^2 - 1 \right] - \frac{m}{I} r_{\text{cm}} L \cos \phi_i \partial_t^2 \Phi', \quad [\text{S28}]$$

plus the corresponding equations for the metronome angles  $\psi_i$  on swing  $B$ .

**Summary.** The resulting governing equations may be further cast into a simpler form amenable to physical interpretation of parameters by introducing the rescaled time  $\tau = \omega t$ :

$$\partial_\tau^2 \Phi' = -\left( \frac{\Omega}{\omega} \right)^2 \Phi' + \frac{\kappa}{\omega^2} (\Psi' - \Phi') - \mu_s \partial_\tau \Phi' - \frac{x_0}{L} \sum_{j=1}^N \partial_\tau^2 \sin \phi_j, \quad [\text{S29}]$$

$$\partial_\tau^2 \Psi' = -\left( \frac{\Omega}{\omega} \right)^2 \Psi' + \frac{\kappa}{\omega^2} (\Phi' - \Psi') - \mu_s \partial_\tau \Psi' - \frac{x_0}{L} \sum_{j=1}^N \partial_\tau^2 \sin \psi_j, \quad [\text{S30}]$$

$$\partial_\tau^2 \phi_i = -\sin \phi_i - \mu_m \partial_\tau \phi_i \left[ \left( \frac{\phi_i}{\theta_0} \right)^2 - 1 \right] - \frac{\omega^2 L}{g} \cos \phi_i \partial_\tau^2 \Phi', \quad [\text{S31}]$$

$$\partial_\tau^2 \psi_i = -\sin \psi_i - \mu_m \partial_\tau \psi_i \left[ \left( \frac{\psi_i}{\theta_0} \right)^2 - 1 \right] - \frac{\omega^2 L}{g} \cos \psi_i \partial_\tau^2 \Psi', \quad [\text{S32}]$$

where we have dropped the primed notation in the main text. The rescaled parameters are

$$\mu_m \equiv \frac{\nu_m}{I\omega},$$

$$\mu_s \equiv \frac{\nu_s}{M\omega},$$

$$\omega^2 \equiv \frac{mg r_{\text{cm}}}{I},$$

$$\Omega^2 \equiv \frac{g}{L},$$

$$\kappa \equiv \frac{k}{ML^2},$$

$$x_0 \equiv \frac{m r_{\text{cm}}}{M},$$

where  $x_0$  is the distance scale of the swing motion.

Although the model captures the synchronization and chimera behavior qualitatively, exact quantitative agreement cannot be expected due to inevitable approximations in describing the metronome dynamics. Specifically, the van der Pol term describing the metronome escapement is ad hoc; small-scale variations in the center mass motion of the single-metronome swing system are neglected (Eq. S24). Other sources of the discrepancy may be found in the parametrization of the first and second moments of the metronome pendulum mass. Nevertheless, the model captures all physical aspects of our experimental system very well.

### Numerical Simulations

The model is a differential algebraic equation (DAE) (8) with  $4N + 4$  variables. For numerical integration, we have used Mathematica (Wofram Research), which provides solvers for (implicit) DAEs (including solvers for the initial conditions that need to be consistent with the differential equations to be solved). Mathematica's DAE solver is based on the Implicit Differential-Algebraic (IDA) solver (9–11).

Rescaling the swing angles by  $\tilde{\Phi} = L/x_0 \Phi$  in the equations is advantageous for numerical integration:

$$\partial_\tau^2 \tilde{\Phi} = \frac{\kappa}{\omega^2} (\tilde{\Psi} - \tilde{\Phi}) - \frac{\Omega^2}{\omega^2} \tilde{\Phi} - \mu_s \partial_\tau \tilde{\Phi} - \sum_{j=1}^N \partial_\tau^2 \sin \phi_j, \quad [\text{S33}]$$

$$\partial_\tau^2 \tilde{\Psi} = \frac{\kappa}{\omega^2} (\tilde{\Phi} - \tilde{\Psi}) - \frac{\Omega^2}{\omega^2} \tilde{\Psi} - \mu_s \partial_\tau \tilde{\Psi} - \sum_{j=1}^N \partial_\tau^2 \sin \psi_j, \quad [\text{S34}]$$

$$\partial_\tau^2 \phi_i = -\sin \phi_i - \mu_m \partial_\tau \phi_i \left[ \left( \frac{\phi_i}{\theta_0} \right)^2 - 1 \right] - \beta \cos \phi_i \partial_\tau^2 \tilde{\Phi}, \quad [\text{S35}]$$

$$\partial_\tau^2 \psi_i = -\sin \psi_i - \mu_m \partial_\tau \psi_i \left[ \left( \frac{\psi_i}{\theta_0} \right)^2 - 1 \right] - \beta \cos \psi_i \partial_\tau^2 \tilde{\Psi}. \quad [\text{S36}]$$

Here, we have introduced the following nondimensional parameters:

$$\mu_m \equiv \frac{\nu_m}{I \omega},$$

$$\mu_s \equiv \frac{\nu_s}{M \omega},$$

$$\beta \equiv \frac{x_0 \omega^2}{g} = \frac{(m r_{\text{cm}})^2}{M I} = \frac{m}{M} \cdot \frac{m r_{\text{cm}}^2}{I},$$

$$\omega_r^2 \equiv \frac{\Omega^2}{\omega^2} = \frac{g}{L \omega^2} = \frac{I}{m L r_{\text{cm}}},$$

$$\chi \equiv \frac{\kappa}{\omega^2} = \frac{k}{M} \left( \frac{l}{L} \right)^2 \frac{I}{m g r_{\text{cm}}}.$$

Parameters  $I$  and  $r_{\text{cm}}$  are parameterized as functions of the nominal frequency  $f$  (Eqs. S7, S9, and S10), which is one of the two control parameters in our experiment. These parameters may be interpreted as follows. The ratio of the first and second moments of the metronome and swing masses is  $\beta$ , and it de-

termines how much energy is transferred between the metronome and swing, thus controlling the coupling strength between metronomes in a single population;  $\chi$  is the spring coupling strength between the populations. The swing energy is dissipated at rate  $\mu_s$ . The metronome is characterized by  $\mu_m$ , and the standard displacement angle is characterized by  $\theta_0$ , which tunes how nonlinear the metronome is (note that  $\theta_0$  can only be scaled into the metronome and swing angles if  $\theta_0 \ll 1$ ).

Parameters in our experiment are typically as follows:

$$\begin{aligned} N &= 15 \\ m_s &= 0.915 \text{ kg} \\ m_m &= m_{\text{box}} + m_p + m_{\text{bob}} = 0.093 \text{ kg} \\ M &= m_s + N \times m_m = 2.31 \text{ kg} \\ m &= m_p + m_{\text{bob}} = 0.028 \text{ kg} \\ g &= 9.81 \text{ m} \cdot \text{s}^{-2} \\ L &= 0.22 \text{ m} \\ L_p &= 0.2 \text{ m} \\ l &= 0.15 \text{ m} \quad (0.05 \text{ m} \leq l \leq 0.25 \text{ m}) \\ f &= 160 \text{ bpm} \quad (40 \text{ bpm} \leq f \leq 208 \text{ bpm}) \\ \omega_n &= 8.38 \text{ rad} \cdot \text{s}^{-1} \\ \omega &= 8.61 \text{ rad} \cdot \text{s}^{-1} \\ \theta_0 &= 19^\circ = 0.33 \text{ rad} \\ \Phi^* &= 8.5^\circ = 0.15 \text{ rad} \\ k &= 68 \text{ N} \cdot \text{m}^{-1} \\ \nu_s &\sim 0.1 \text{ kg} \cdot \text{s}^{-1} \\ \nu_m &= 1.8 \times 10^{-6} \text{ kg} \cdot \text{m}^2 \cdot \text{s}^{-1}. \end{aligned}$$

Note that  $\nu_s$  and  $\nu_m$  have dissimilar units. The value of  $\mu_m$  is based on values obtained from Pantaleone (2). With the above values, the nondimensional parameters are of the following order:

$$\begin{aligned} \mu_s &= 0.00016 \\ \mu_m &= 0.011 \\ \beta &= 0.0005 \\ \omega_r^2 &= 0.6 \\ \chi &= 0.092, \end{aligned}$$

which are roughly representative of our experiment (Figs. 2 and 3).

**Initial Conditions.** Initial conditions were prepared to be consistent with three types of states: (i) fully synchronized consistent with the in-phase (IP) mode, (ii) with the antiphase (AP) mode, or (iii) with chimera states, where only one population is synchronized and the other is desynchronized. For the synchronized states (i and ii), we use

$$\phi_i(0) = 2\theta_0$$

$$\partial_\tau \phi_i(0) = 0$$

$$\psi_i(0) = \pm 2\theta_0$$

$$\partial_\tau \psi_i(0) = 0, \quad i = 1 \dots N, \quad [\text{S37}]$$

where the minus signs apply for the AP mode. For chimera states (iii), the desynchronized population is randomized as follows:

$$\phi_i(0) = 2\theta_0(r_i - 1/2)$$

$$\phi'_i(0) = 2\theta_0(r_i - 1/2), \quad i = 1 \dots N, \quad [\text{S38}]$$

where  $r_i$  is a random number in  $[0, 1]$ . One may then assign average angles and angular velocities to the synchronized pop-

ulation so that the kinetic and potential energy of metronome populations  $A$  and  $B$  matches. For all three types of conditions, the swings are released from their equilibrium positions with zero momentum:

$$\tilde{\Phi}(0) = \tilde{\Psi}(0) = 0$$

$$\partial_\tau \tilde{\Phi}(0) = \partial_\tau \tilde{\Psi}(0) = 0. \quad [\text{S39}]$$

**Integration of Model Equations and Parameter Sweeps.** Simulations were carried out with identical metronomes until a (quasi-)stationary state was reached ( $\tau \sim 12'000$ ). The stability diagram in the main text (Fig. 44) was obtained by fixing the nominal metronome frequency  $f$  (138, 160, 184, and 208 bpm) and then gradually increasing the effective spring rate  $\kappa$  (using the same parameters as in the experiment and  $n = 15$  metronomes per swing). For each parameter step of the sweep, simulations were reinitialized, with the initial conditions consistent with the IP, AP, or chimera state as listed above.

The resulting phase diagram does not represent observed states in comprehensive detail but is a simplified view of a complex spectrum of states. IP and AP states always represent perfectly synchronized states; the region of a chimera-like state comprises any states in which at least one population is perfectly synchronized. A detailed stability analysis would be needed to uncover further questions, including precise stability properties and bifurcation scenarios of these states.

**Further Simulations.** To extend our experiments, we also carried out simulations for situations that are not possible (or are very difficult) to achieve experimentally. We mainly carried out two

sets of extended simulations: (i) to investigate the effect of dissipation (in this case, the friction of the swing) on the chimera behavior and (ii) to study the transition between the different regions by using an increased number of metronomes to reduce finite size fluctuations.

**Effect of swing friction  $\nu_s$ .** We sought to investigate the effect of swing friction on the chimera region in simulations. For these simulations, we use parameters as listed in the previous section and vary the swing friction by three orders of magnitude from  $\nu_s = 0.031$  kg/s to  $\nu_s = 3.1$  kg/s. A series of phase diagrams are plotted in Fig. S6 for increasing values of  $\nu_s$ . Although the qualitative behavior remains the same in all cases, it can be seen that with increasing friction, the width of the region with unsynchronized (chimera-like) behavior increases, further demonstrating that the difference between the experimental and numerical phase diagrams in the main text (Fig. 3) could be due to such effects.

**Simulations with  $N = 64$  metronomes.** The transition of chimeras between AP and IP regions is investigated with an increased number of metronomes to reduce finite size fluctuations (Fig. 4). The modification of the parameters as listed below corroborates that the chimera phenomenon is not specific to a small-parameter region:

$$\begin{aligned} f &= 184 \\ \omega_r^2 &= 0.38 \\ \chi &= 0.294 \dots 0.266 \\ \beta &= 0.00031 \\ \mu_s &= 0.002 \\ \mu_m &= 0.0092 \\ \theta_0 &= 0.66. \end{aligned}$$

1. Bennett M, Schatz M, Wiesenfeld K (2002) Huygen's clocks. *Proc R Soc Lond A Math Phys Sci* 458(2019):563–579.
2. Pantaleone J (2002) Synchronization of metronomes. *American Journal of Physics* 70(10):992–1000.
3. Strogatz SH (1994) *Nonlinear Dynamics and Chaos* (Perseus Books, Reading, MA).
4. Pikovsky A, Rosenblum M, Kurths J (2001) *Synchronization. A Universal Concept in Nonlinear Sciences* (Cambridge Univ Press, New York).
5. Kralemann B, Cimponeriu L, Rosenblum M, Pikovsky A, Mrowka R (2008) Phase dynamics of coupled oscillators reconstructed from data. *Phys Rev E Stat Nonlin Soft Matter Phys* 77(6 Pt 2):066205.
6. Belykh VN, Pankratova EV (2010) Chaotic dynamics of two van der Pol-Duffing oscillators with Huygens coupling. *Regular and Chaotic Dynamics* 15(2-3):274–284.
7. Ulrichs H, Mann A, Parlitz U (2009) Synchronization and chaotic dynamics of coupled mechanical metronomes. *Chaos* 19(4):043120.
8. Campbell, SL et al. (2008) Scholarpedia: Differential-algebraic equations. Available at [www.scholarpedia.org/article/Differential-algebraic\\_equations](http://www.scholarpedia.org/article/Differential-algebraic_equations).
9. Hindmarsh A, Taylor A (1999) *User Documentation for IDA: A Differential-Algebraic Equation Solver for Sequential and Parallel Computers*. Lawrence Livermore National Laboratory. Technical report. Available at <http://acts.nersc.gov/sundials/documents/237206.pdf>.
10. Wolfram Research (2013) Mathematica: IDA method for NDSolve. Available at <http://reference.wolfram.com/mathematica/tutorial/NDSolveIDAMethod.html>. Accessed May 28, 2013.
11. Wolfram Research (2013) Mathematica: Numerical solution of differential-algebraic equations. Available at <http://reference.wolfram.com/mathematica/tutorial/NDSolveIntroductoryTutorialDAEs.html>. Accessed May 28, 2013.



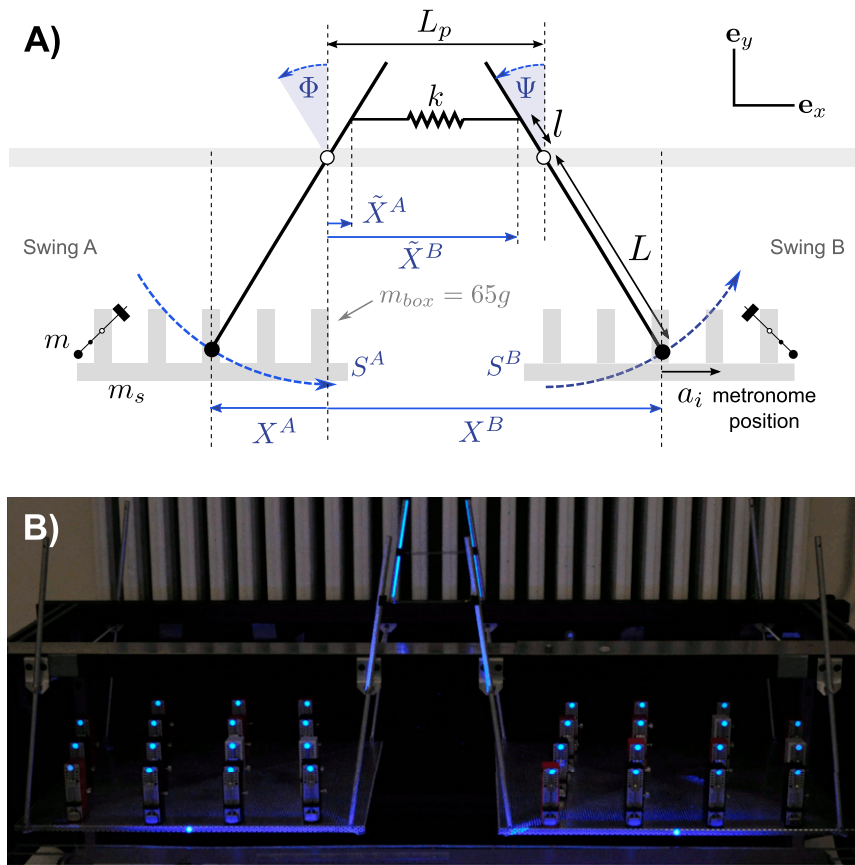


**Fig. 51.** System with two swings coupled with two identical springs. Each swing carries  $N = 15$  metronomes. (A) Schematics of the experimental setup. (B) Each swing and the top of each pendulum are marked with fluorescent dots, which are highlighted using UV light. Note that the center mass motion occurs in the opposite direction of these dots because the center mass of the metronome pendulum lies below its pivot (Fig. 53).

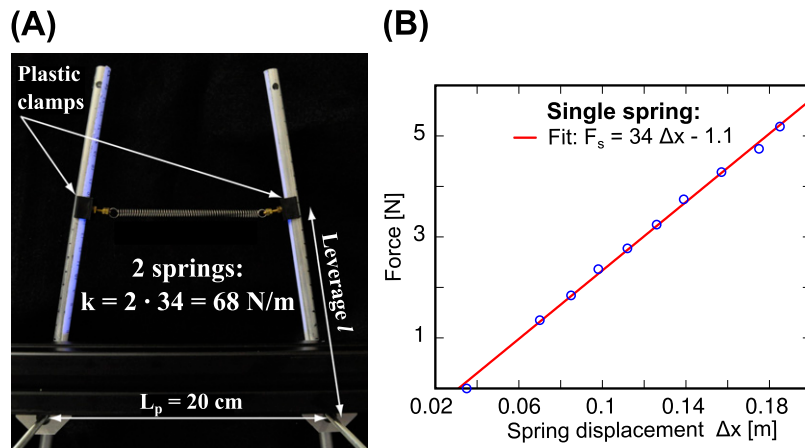


**Fig. 52.** (A) Two springs mediate the coupling between the two adjacent rod pairs at the front and back sides of the swings (back side shown). The springs are firmly connected to the rods with plastic clamps. (B) Spring constant of a single spring in our setup has been measured with a value of  $34 \text{ N} \cdot \text{m}^{-1}$ ; thus, the resulting total spring rate is  $k = 68 \text{ N} \cdot \text{m}^{-1}$  with two springs attached.

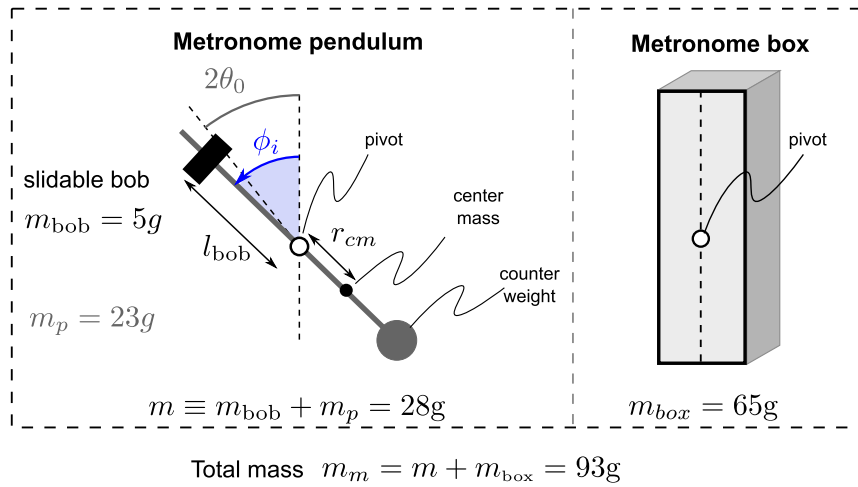


**Fig. S3.** Metronome has two components: the metronome pendulum of mass  $m$ , which constitutes the dynamically active element of the metronome system (Left), and the metronome box of mass  $m_{box}$ , which is fixed with respect to the swing system (Right). The state of the metronome pendulum is described by its displacement angle  $\phi_i$  and its angular velocity  $\partial_t \phi_i$ . Half of the standard displacement angle of the pendulum (single uncoupled pendulum) is represented by  $\theta_0$ . The pendulum is composed of a counterweight (gray disk) and rod (gray) of mass  $m_p$ . The frequency of the pendulum is adjusted by sliding the bob mass  $m_{bob}$  (black rectangle) above the pivot (empty circle) up and down, resulting in an alteration of the pendulum's center mass position  $r_{cm}$ , which always lies below the pivot.

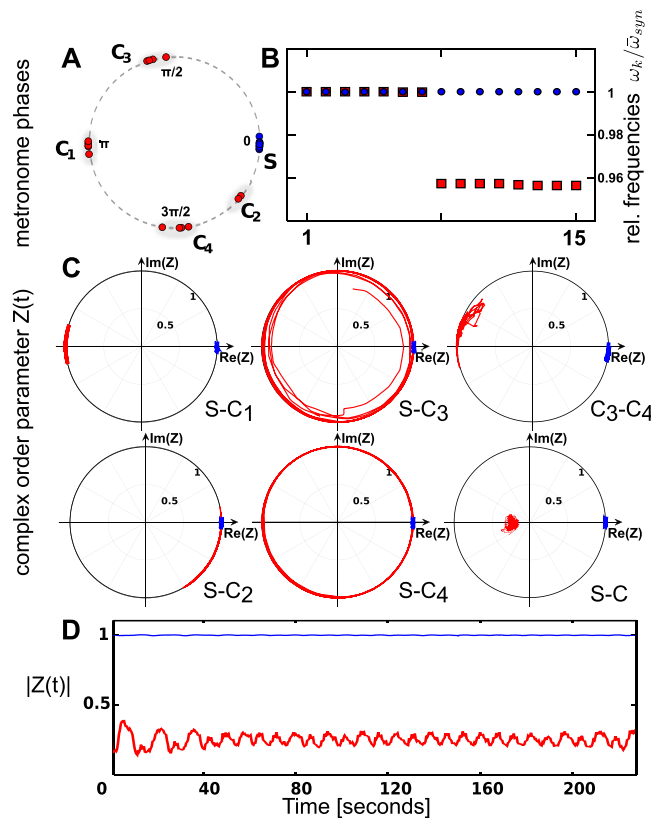


**Fig. S4.** Analysis of a (partially) phase-clustered state obtained for interpopulation coupling of  $\kappa = 29.56$  and a nominal metronome frequency  $f = 184$  bpm. (A) Phases of individual metronomes [red, asynchronous population; blue, synchronous population (S)]. Phases belonging to different clusters are shaded in gray and labeled  $C_k$ . (B) Frequencies averaged over the last 50% of the observation time,  $\bar{\omega} = \langle \omega \rangle_t$ , relative to the average frequency  $\bar{\omega}_{syn}$  of the synchronized population; red and blue populations are superposed. (C) Panels S- $C_k$  show the complex order parameter evolution of the subpopulations  $C_k$  (where  $k=1,2,3,4$ ) relative to order parameter of the synchronized population S (i.e., the angular component is subtracted - thus a view in the co-rotating frame is shown); in addition, panel S-C shows the order parameter representing the entire asynchronous, clustered population. (D) Time evolution of the magnitude of the order parameters of the synchronous and asynchronous populations.

Figure 2 consists of five subplots (A-E) showing the relationship between Spring coupling  $\kappa$  (y-axis, 0 to 50) and Metronome frequency  $f$  [bpm] (x-axis, 140 to 210). Each plot shows a green shaded region representing the range of  $\kappa$  values for a given  $f$ , with a black line indicating the mean and error bars. The plots are labeled with 'IP' (red) and 'AP' (blue) regions. A box in each plot indicates the value of  $\nu_c$ .

- A)**  $\nu_c = 0.031 \text{ kg/s}$ . The green region is narrow, starting around  $\kappa = 5$  at  $f = 140$  and reaching  $\kappa \approx 45$  at  $f = 210$ .
- B)**  $\nu_c = 0.093 \text{ kg/s}$ . The green region is wider than in A, reaching  $\kappa \approx 45$  at  $f = 210$ .
- C)**  $\nu_c = 0.31 \text{ kg/s}$ . The green region is wider than in B, reaching  $\kappa \approx 45$  at  $f = 210$ .
- D)**  $\nu_c = 0.93 \text{ kg/s}$ . The green region is wider than in C, reaching  $\kappa \approx 45$  at  $f = 210$ .
- E)**  $\nu_c = 3.1 \text{ kg/s}$ . The green region is the widest, reaching  $\kappa \approx 45$  at  $f = 210$ .

**Table S1. Typical equilibrium angles with varying spring lever  $l$**

$l$ , cm	$\Phi^*$ , °
7	5.3
10	6.9
11	7.3
14	8.2
20	9.2
23	9.0

Movie S1





**Movie S2.** Experimental observation of an in-phase synchronization mode (i.e., the 2 swings carrying the metronomes are synchronized in-phase). The motion of each metronome pendulum is highlighted using UV light.

[Movie S2](#)



**Movie S3.** Experimental observation of an anti-phase synchronization mode (i.e. the 2 swings carrying the metronomes are synchronized exactly 180 degrees out-of-phase). The motion of each metronome pendulum is highlighted using UV light.

[Movie S3](#)